AGU100 ADVANCING EARTH AND SPACE SCIENCE

Geophysical Research Letters

RESEARCH LETTER
10.1029/2018GL080455

Key Points:
- The Sentinel-3 Ocean and Land Colour Instrument (OLCI) can capture the spectral signals of chlorophyll-*a* pigment generated by ice algae
- The spatial pattern of algal abundance characterized by the reflectance ratio R_{709nm}/R_{673nm} is highly consistent with field measurements
- The dark ice presence and ice algal abundance in southwest Greenland are closely linked to meltwater production and surface runoff

Supporting Information:
- Supporting Information S1
- Data Set S1

Correspondence to:
S. Wang and M. Tedesco,
swang@ldeo.columbia.edu;
cryocity@gmail.com

Citation:
Wang, S., Tedesco, M., Xu, M., & Alexander, P. M. (2018). Mapping ice algal blooms in southwest Greenland from space. *Geophysical Research Letters*, *45*. https://doi.org/10.1029/2018GL080455

Received 12 SEP 2018
Accepted 19 OCT 2018
Accepted article online 25 OCT 2018

Mapping Ice Algal Blooms in Southwest Greenland From Space

Shujie Wang[1], Marco Tedesco[1,2], Min Xu[3], and Patrick M. Alexander[1,2]

[1]Lamont-Doherty Earth Observatory, Columbia University, Palisades, NY, USA, [2]NASA Goddard Institute for Space Studies, New York, NY, USA, [3]Department of Geography, University of Alabama, Tuscaloosa, AL, USA

Abstract Quantifying the distribution and abundance of ice algae is fundamental for understanding the evolving processes of algal blooms in supraglacial environments, particularly over the Greenland ice sheet, given the role of algal impurities in modulating surface albedo and meltwater production. Field observations of ice algae in Greenland are very limited over space and time. Here we show for the first time the regional variability in algal abundance across the *dark* zone in southwest Greenland, derived from Sentinel-3 images acquired during the summertime in 2016 and 2017. We demonstrate the capacity of Sentinel-3 imagery to characterize the spatial pattern of algal abundance using the reflectance ratios between 709- and 673-nm bands, highly consistent with field measurements. The estimated algal abundance reveals a significant linear growth pattern of algal population with time after the peak of dark ice presence, shown to be tightly linked to surface runoff and meltwater production.

Plain Language Summary Ice algae bloom plays an important role in enhancing the surface melting of the Greenland ice sheet. It has been challenging to monitor the development of ice algae at a regional scale with temporally frequent observations. In this study, we map the time series of algal abundance over southwest Greenland from space for the first time, by utilizing the advanced capability of Sentinel-3 satellites in detecting chlorophyll-*a*, a typical pigment generated by algae. The spatial pattern of algal abundance characterized by Sentinel-3 imagery is highly consistent with field measurements. Our analysis reveals the widespread proliferation of algae on bare ice from late July to mid-August, with increasing algal population over time after the peak of surface runoff and meltwater production. Incorporating the algal distribution derived from satellite data into regional climate models is expected to improve the projection of future mass balance over the Greenland ice sheet.

1. Introduction

Increased surface meltwater runoff has recently become the predominant process for mass loss of the Greenland ice sheet (GrIS; Hanna et al., 2013; Shepherd et al., 2012; Smith et al., 2015). Surface albedo, modulated by snow grain size and light-absorbing impurities (LAI), is a primary control on meltwater production (Tedesco et al., 2011). Albedo reduction could increase the amount of solar energy absorbed by snow and ice, thus enhancing surface ablation (Tedesco et al., 2011). Recent studies (e.g., Box et al., 2012; Stroeve, 2001; Tedesco, Box, et al., 2016; Tedesco, Doherty, et al., 2016) have revealed a significant decrease in surface albedo over the GrIS, particularly in southwest Greenland with a recurring *dark* zone every summer (Shimada et al., 2016; Tedstone et al., 2017; Wientjes & Oerlemans, 2010).

Surface darkening in Greenland is tightly coupled to the presence of LAI including mineral dust (Wientjes et al., 2011), black carbon (Goelles & Bøggild, 2017), cryoconite (Chandler et al., 2015), and algal blooms (Stibal et al., 2015, 2017; Williamson et al., 2018; Yallop et al., 2012). These LAI affect the albedo at ultraviolet and visible wavelengths (Tedesco, Box, et al., 2016; Tedesco, Doherty, et al., 2016; Warren, 1982). Field surveys indicate that the biologically active impurities caused by ice algal assemblages play a crucial role in darkening the surface ice in Greenland (Ryan et al., 2018; Stibal et al., 2017; Williamson et al., 2018; Yallop et al., 2012). Abundant algae from the group Zygnematophyceae were found within the upper few centimeters of surface ice (Williamson et al., 2018; Yallop et al., 2012). The algae produce a purpurogallin-type phenolic pigment that absorbs excessive ultraviolet and visible radiation in supraglacial environments and is suggested to be closely related to the albedo reduction of surface ice (Remias et al., 2012). Given the importance of ice algae in altering the melting conditions, it is fundamental to understand the spatiotemporal evolution of ice algal biomass on the GrIS. However, available information on ice algae in Greenland is limited to a few field

sites (Stibal et al., 2015, 2017; Uetake et al., 2010; Yallop et al., 2012), and the spatial variability of algal biomass at a regional scale remains poorly known.

Ancylonema nordenskioldii and *Mesotaenium berggrenii* of the green microalgae are the primary species found on bare ice surface in southwest Greenland (Stibal et al., 2015, 2017; Uetake et al., 2010; Williamson et al., 2018; Yallop et al., 2012). These algae produce typical pigments of green microalgae, such as chlorophyll-*a* and chlorophyll-*b*, beta-carotene, lutein, and xanthophyll. Chlorophyll-*a*, the dominant pigment detected in field samples (Williamson et al., 2018; Yallop et al., 2012), exhibits unique spectral signatures in the red and near-infrared (NIR) wavelengths. Strong correspondence of chlorophyll and carotenoid concentrations with algal biomass has been demonstrated through field measurements (Williamson et al., 2018). In situ spectral and hyperspectral data indicate that the surface ice coupled with a high algal abundance presents the spectral characteristics of chlorophyll-*a* (Painter et al., 2001; Stibal et al., 2017). These features hint at an enormous potential of Sentinel-3 satellites in monitoring the development of ice algal blooms from space. The successful launch of Sentinel-3A in 2016 signaled the advent of a new era for studying optically complex aquatic systems (Malenovský et al., 2012). The satellite is equipped with the Ocean and Land Colour Instrument (OLCI) to measure the reflected solar radiation in 21 spectral bands. OLCI has improved capabilities for retrieving chlorophyll content owing to its advanced band designations in the red and NIR bands, as compared to previous multispectral satellite sensors such as Moderate Resolution Imaging Spectroradiometer (MODIS), Landsat Thematic Mapper, and Operational Land Imager. Broadband data are usually inadequate for quantifying chlorophyll content, and narrowband data with a bandwidth of 10 nm or less are often required (Beck et al., 2016; Blackburn, 2007). The wavelength resolution of those Sentinel-3 bands designed specifically for chlorophyll retrieval is 7.5 or 10 nm, which is sufficient to identify chlorophyll-*a* spectral features.

In this study, we use a time series of Sentinel-3 OLCI images to study the spatiotemporal evolution of ice algal blooms in southwest Greenland (65–70°N, 46–51°W) during the summer seasons of 2016 and 2017. Note that we focus on the algal development within the dark ice zone. We first delineate the spatial extent of dark ice using a thresholding method (Shimada et al., 2016; Tedstone et al., 2017). We then estimate the algal abundance over dark ice by combining the spectral characteristics of chlorophyll-*a* with field measurements. We also examine the influences of meteorological factors as well as surface melting on the changes of dark ice and algal abundance using the outputs of a regional climate model.

2. Data and Methods

2.1. Satellite Data

We used a total of 75 Sentinel-3A OLCI images acquired during the summertime in 2016 and 2017. Each OLCI image has a swath of 1,270 km and a spatial resolution of 300 m. OLCI collects data in 21 bands at the wavelength range of 400–1,020 nm, with bandwidths between 2.5 and 40 nm (Table S1 in the supporting information). The red and NIR bands that are sensitive to chlorophyll-*a* content, including 665, 673, 681, and 709 nm, have high spectral resolutions of 7.5 or 10 nm. The full resolution level-1B product, containing the radiometrically calibrated top of atmospheric radiances for 21 spectral bands, was used for our analysis. The selected 75 images are either cloud-free or minimally contaminated by clouds over the study area. We performed atmospheric correction to convert the top of atmospheric radiances to surface reflectances using the MODTRAN-based Fast Line-of-sight Atmospheric Analysis of Hypercubes (Anderson et al., 2002). The sub-Arctic summer MODTRAN model was selected to correct for the column water vapor effect. The water vapor content was retrieved using the OLCI 940-nm band as a water absorption channel and the 885-nm band as a water reference channel. The rural aerosol model was used to remove the aerosol effect. The spectral filter function required for atmospheric correction was compiled using the OLCI spectral response functions provided by the European Space Agency (https://sentinel.esa.int/web/sentinel/technical-guides/sentinel-3-olci/olci-instrument/spectral-response-function-data).

We also used MODIS/Terra daily surface reflectance data product (MOD09GA Version 6) and daily snow cover data product (MOD10A1 Version 6; https://modis.gsfc.nasa.gov/data/dataprod/). The spatial resolution of these data sets is 500 m. The MOD09GA data include atmospherically corrected spectral reflectances for the MODIS bands 1 to 7. The MOD10A1 data were utilized to remove the cloud pixels from the MOD09GA

images. The MODIS images were resampled to 300 m using the nearest neighbor method to be consistent with the spatial resolution of Sentinel-3A OLCI images.

2.2. Dark Ice Mapping

We use a thresholding method to map dark ice from the atmospherically corrected Sentinel-3 OLCI data. Ocean and tundra were excluded using the land and ocean classification mask from the MEaSUREs Greenland Ice Mapping Project (Howat et al., 2014).

The MODIS bands of 841–876 and 620–670 nm were previously used for dark ice mapping by Shimada et al. (2016) and Tedstone et al. (2017). They first used $R_{620\text{-}670nm} < 0.4$ to differentiate bare ice from snow and then applied the threshold of 0.4 or 0.45 to the band of 620–670 nm to identify dark ice within the bare ice area. Here we use the Sentinel-3 OLCI bands of 865 and 620 nm to delineate the bare ice and dark ice area. Similar to the MODIS method, we extracted the bare ice area using $R_{865nm} < 0.6$. To detect dark ice, we considered the difference of central wavelength and bandwidth between the MODIS 620- to 670-nm band and the Sentinel-3 620-nm band. We implemented threshold optimization by iteratively comparing the derived time series of dark ice using different thresholds to the Sentinel-3 620-nm band with the MODIS-derived time series (see Text S1). We found that the threshold of 0.48 (applied to the 620-nm band) can best match the MODIS method.

After applying the thresholds, we found that supraglacial lakes could be misclassified as dark ice due to the low reflectivity of water. We removed the lakes using a modified normalized difference water index (NDWI; Yang & Smith, 2013). This index is the normalized ratio of the blue and red bands (Text S2), which has been proven to be more effective for detecting supraglacial water than the traditional NDWI (Yang & Smith, 2013). For each Sentinel-3 image, we calculated the modified NDWI using the bands of 490 and 665 nm. By trial and error, most of the lakes were removed by applying the threshold of 0.15 to the NDWI.

2.3. Spectral Ratio Index

As the primary photosynthetic pigment, the chlorophyll-*a* content is generally used as a proxy for algal biomass (e.g., Beck et al., 2016; Matthews, 2011). Chlorophyll-*a* has unique spectral characteristics, with two absorption valleys around 440 (blue) and 670 nm (red) and two reflection peaks around 550 (green) and 710 nm (NIR). The surface reflectance ratios between the NIR and red bands are commonly used to estimate the chlorophyll-*a* concentration in aquatic systems by combining remote sensing data with in situ measurements (Blondeau-Patissier et al., 2014; Gitelson, 1992; Gitelson et al., 2009; Gower et al., 2005; Ruddick et al., 2001). As the surface reflectances at 709 and 673 nm are highly sensitive to the variations in chlorophyll-*a* content, we suggest it is plausible to use the reflectance ratio R_{709nm}/R_{673nm} as an index to characterize the relative abundance of ice algae from remote sensing data in the absence of in situ measurements. This idea is further supported by field data measured over dark ice in Greenland. In this regard, Stibal et al. (2017) collected in situ measurements of algal abundance (cells/ml) and reflectance spectra at a site in southwest Greenland during the summer of 2014. The spectral reflectances indicate that the dark ice with a high algal abundance exhibits chlorophyll-*a* signatures, with a reflectance peak around 709 nm and an absorption feature around 673 nm. In our study, we evaluated the statistical relationship between the algal abundance and reflectance ratio based on the published field data set of Stibal et al. (2017). We tested three chlorophyll-related ratio indexes, R_{710nm}/R_{660nm}, R_{710nm}/R_{670nm}, and R_{710nm}/R_{680nm}, using the samples collected between 1 July and 8 August by Stibal et al. (2017). The results indicate that the binary logarithm of algal abundance is positively correlated with the ratio R_{710nm}/R_{670nm}, with a Pearson's r of 0.57 and p value less than 0.001. The correlations with the remaining two indexes were less significant. Accordingly, we calculated the ratio index for each dark ice pixel using the OLCI bands 11 (708.25 nm) and 9 (673.25 nm).

2.4. MAR Regional Climate Model

We use meteorological variables and surface mass balance components simulated by the Modèle Atmosphérique Régionale (MAR; Fettweis et al., 2017) to examine the influence of those environmental factors on the dynamics of dark ice and ice algae. MAR generates regional-scale simulations of surface mass balance and energy processes over the Greenland and Antarctic ice sheets, with a spatial resolution of 7.5 km over the GrIS. It combines the atmospheric model of Gallée and Schayes (1994) with the Soil Ice Snow Vegetation Atmosphere Transfer scheme of De Ridder and Gallée (1998), and the boundary conditions are

prescribed by the European Centre for Medium-Range Weather Forecasts Interim Reanalysis (Dee et al., 2011) or global climate model outputs. The model performance has been extensively evaluated over the GrIS (e.g., Alexander et al., 2014; Fettweis et al., 2013, 2017). We used the daily simulation outputs for June, July, and August in 2016 and 2017, including the variables of near-surface air temperature, shortwave downward radiation, longwave downward radiation, sensible heat flux, latent heat flux, meltwater production, snowfall, rainfall, and surface runoff of meltwater or rainwater.

3. Results

3.1. Dark Ice Dynamics

Our results indicate the widespread darkening of surface ice in July and August over the ablation zone in southwest Greenland (Figure 1), consistent with the timing of ice algal colonization (Stibal et al., 2017; Williamson et al., 2018; Yallop et al., 2012). The bare ice (including dark ice zone) was exposed inland from the ice margin in June and July, reaching its maximum extent between late July and mid-August (Figures 1 and S1). Although the dark ice area is highly correlated with the bare ice area (Pearson's r is 0.86 for 2016 and 0.88 for 2017), the dark ice area was minimal until 6 July 2016 and 27 July 2017, while bare ice area increased more gradually through the beginning of the summer months. For both years, the development of dark ice was characterized by a rapid expansion at the central part of bare ice zone over a few days in July. Such dramatic pattern also happened in 2011, 2012, and 2014 (Tedstone et al., 2017).

The extents of bare ice and dark ice area were substantially greater in 2016 than in 2017, consistent with the above-average melting record in 2016 (Tedesco, Box, et al., 2016; Tedesco, Doherty, et al., 2016) and the below-average melting in 2017 (Tedesco et al., 2017). The exposure of bare ice reached the altitude of 1,900 m in 2016, whereas in 2017, the bare ice zone was limited to the elevations below 1,600 m (Figures 1a, 1b, and S1). The maximum area of dark ice in 2017 was 109,784 km^2, 32% smaller than that in 2016. Similarly, the maximum area of bare ice in 2017 was 28% less than that in 2016. In addition to the spatial extent, the period with dark ice presence was generally longer in 2016 (Figures 1a–1c), with the peak of dark ice occurring on 22 July, 5 days earlier than the peaking time in 2017 (Figures S1 and S2).

The notable differences in bare ice and dark ice between the years 2016 and 2017 indicate the importance of surface melting and meteorological controls on surface darkening. Figures 1d–1g show the strong correspondence of the areas of bare ice and dark ice with surface runoff and meltwater production as simulated by MAR. The peaking time of bare ice and dark ice area coincided with the maxima of surface runoff and meltwater production. The areal shrinkage of dark ice and bare ice was closely related to snowfall events (Figures 1f and 1g). We examined the correlations of bare ice and dark ice area with various variables modeled by MAR (Figures S3 and S4) and found that for both summers, the dark ice and bare ice areas had statistically significant correlations with surface runoff.

3.2. Ice Algal Distribution

Figure 2a shows that the atmospherically corrected OLCI reflectances are very close to the coincident MODIS surface reflectances at similar bands. However, the OLCI spectra contain more information at the chlorophyll-related wavelengths. The OLCI spectral curve for dark ice has a reflection peak at 709 nm and an absorption feature between 665 and 681 nm. The OLCI spectra are consistent with the in situ data collected by Stibal et al. (2017) for a dark ice site with highly concentrated ice algae detected in surface ice, suggesting a high algal abundance at our sampled dark ice site as well.

We calculated the daily ratio index (R_{709nm}/R_{673nm}) for each dark ice pixel and the average ratio over the darkening period in each summer (Figure S5). The derived ratio index is highly consistent with field measurements of algal abundance (Figure 2b). Stibal et al. (2015) collected samples of surface ice over 14 sites in Greenland from May to September 2013. The sites DS, KAN_L, KAN_M, and KAN_U are within our study area (the locations are shown in Figure 2c). A significant number of algal cells were detected at DS and KAN_M, with an average abundance of 10,621 ± 2,073 and 5,688 ± 3,147 cells/ml through the sampling period, respectively. The algal abundance at KAN_L was much lower, with an average of 66 ± 31 cells/ml. The site KAN_U was dominated by firn, and no significant number of algal cells was found. Correspondingly, the average reflectance ratios for these sites are 1.028 (DS), 0.970 (KAN_L), and 1.018 (KAN_M) in the 2017 summer, and 1.033 (DS) and 1.017 (KAN_M) in the 2016 summer. Williamson et al. (2018) conducted field sampling at

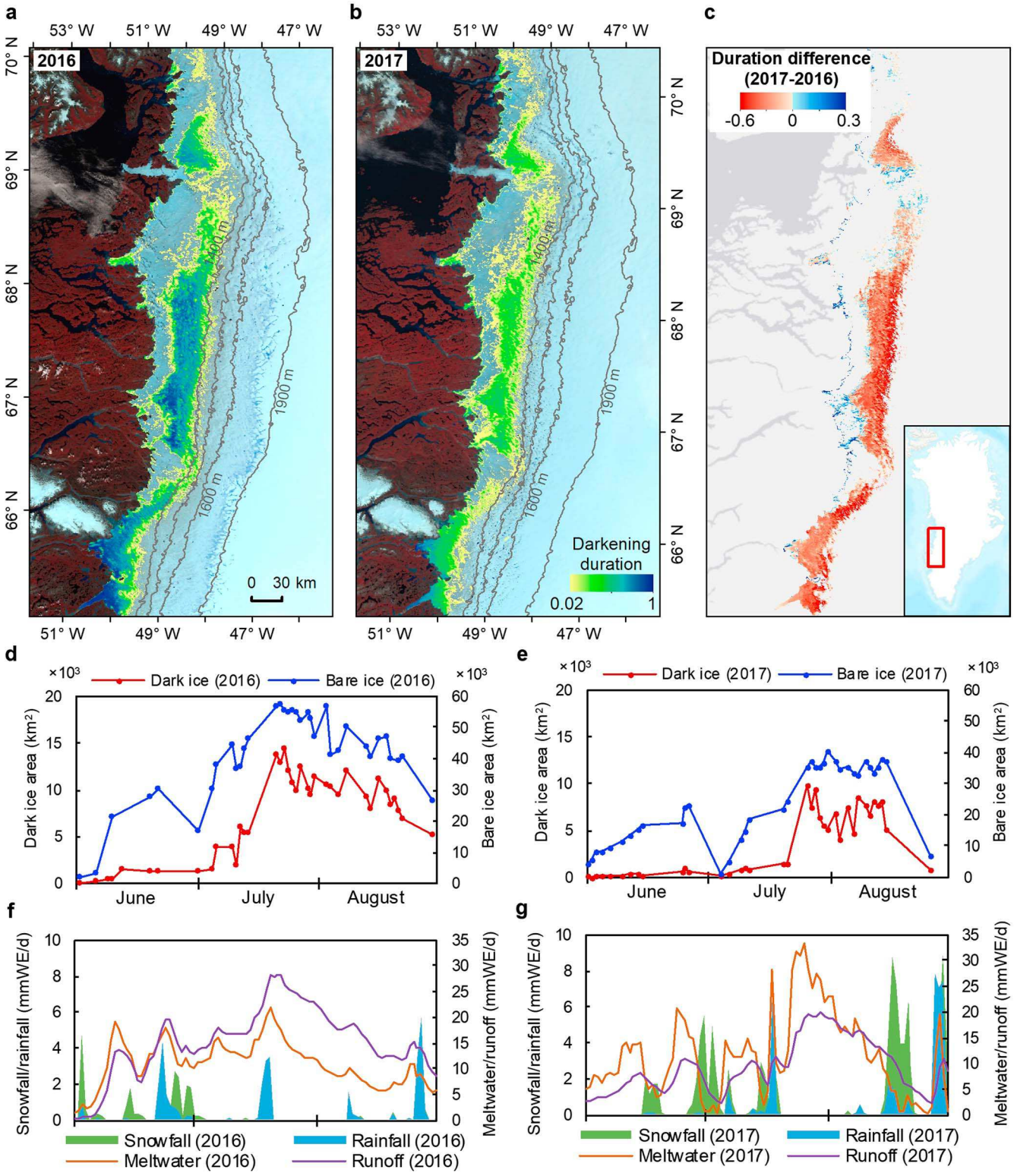

Figure 1. Spatiotemporal variability in dark ice during the summer seasons in 2016 and 2017, along with snowfall, rainfall, meltwater production, and surface runoff simulated by the Modèle Atmosphérique Régionale regional climate model shown in (f) and (g). The darkening duration in (a) and (b) was normalized to the range 0–1, by dividing the number of days with dark ice present by the number of cloudless days (the number of images used for each year). The background images in (a) and (b) are the Sentinel-3 OLCI images (false color composite) acquired on 31 July 2016 and 31 July 2017, respectively. The gray lines in (a) and (b) are elevation contours, showing the upper limits of bare ice and dark ice as indicated by Figure S1. (c) shows the difference of the normalized darkening duration between 2017 and 2016. The time series of the bare ice and dark ice areas during the 2016 and 2017 summer seasons are shown in (d) and (e), respectively.

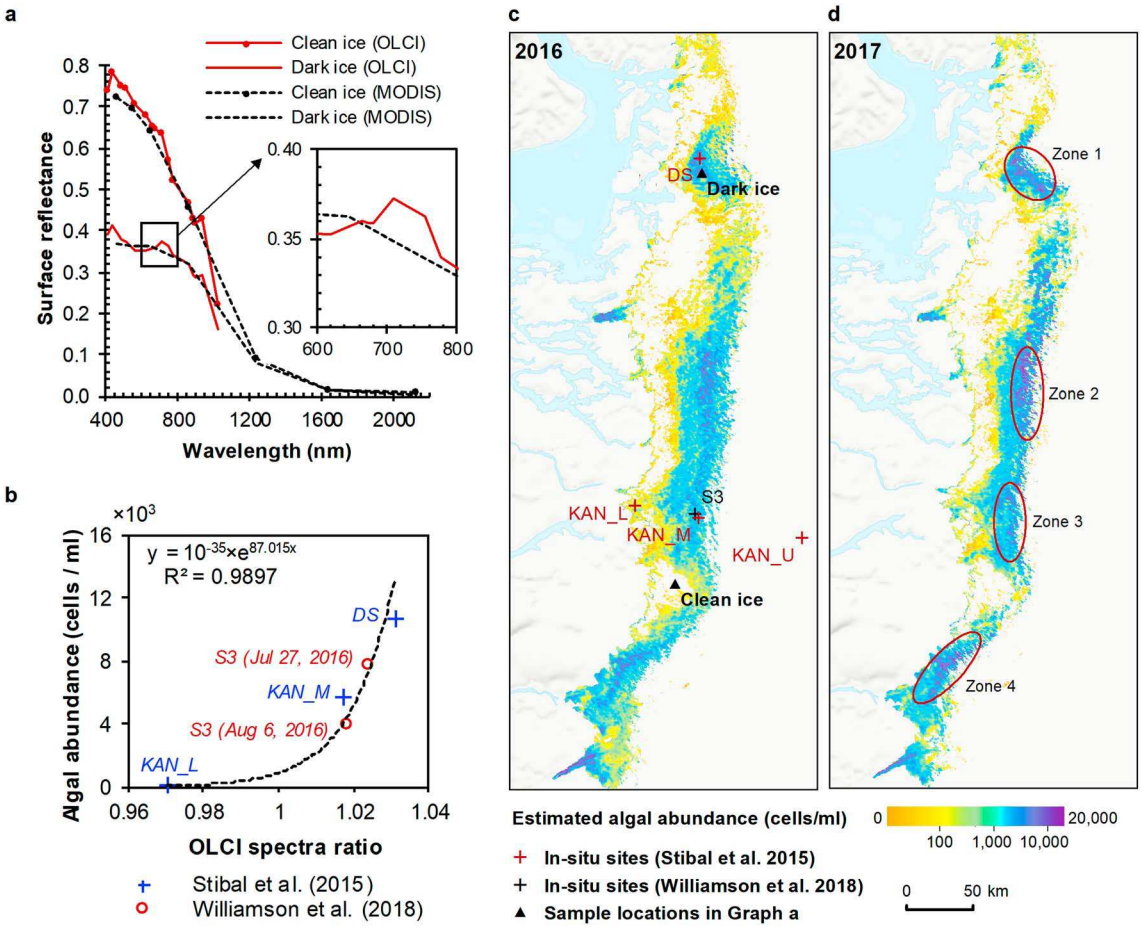

Figure 2. (a) Comparison between MODIS and OLCI spectra for dark ice and clean ice. (b) Spectral reflectance ratio versus algal abundance measured in situ, with the fitted exponential curve. (c) Spatial pattern of the estimated algal abundance for the 2016 summer season, along with the locations of sampled sites. (d) Estimated algal abundance for 2017 and the identified four algal hot spots. MODIS = Moderate Resolution Imaging Spectroradiometer; OLCI = Ocean and Land Colour Instrument.

four sites along two helicopter transects on 27 July and 5 August 2016, respectively. They measured algal cell numbers, biovolume, and species diversity. Among their sampled sites, we identified site S3 as dark ice on both days based on OLCI imagery. The reflectance ratios for this site were 1.024 (27 July) and 1.018 (5 August), corresponding to the algal abundance of 7,656 and 3,906 cells/ml estimated from their Figure 3 (Williamson et al., 2018). Figure 2b shows the field measurements of algal abundance plotted against the reflectance ratios, revealing a statistically significant exponential relationship ($r^2 = 0.989$).

Using the fitted exponential equation, we estimated the average algal abundance for the summer in 2016 and 2017 (Figures 2c and 2d). The derived algal abundance ranged from 0 to 2×10^4 cells/ml, similar to the range of 0–1.6×10^4 cells/ml reported by Williamson et al. (2018). Figure 2d suggests four hot spots that were most likely to be dominated by ice algal assemblages, including Jakobshavn Isbrae Glacier (zone 1), Usugdlup Sermia Glacier and Inugpait Quat Glacier (zone 2), Russell Glacier (zone 3), and Marjorqaq Glacier (zone 4). The extensive occurrence of ice algal blooms at zones 1 and 3 has been confirmed by previous field observations (Stibal et al., 2015, 2017; Williamson et al., 2018; Yallop et al., 2012). Besides, the maps of algal abundance show an altitudinal variation pattern, with a generally increasing trend with elevation. However, due to the limited availability of meltwater for algal growth at further higher elevations, this increasing pattern was limited below the altitude of 1,300 m. Similar patterns were also found on other glaciers such as the Qaanaaq Glacier in northwest Greenland (Uetake et al., 2010) and the Gulkana Glacier in Alaska (Takeuchi, 2001).

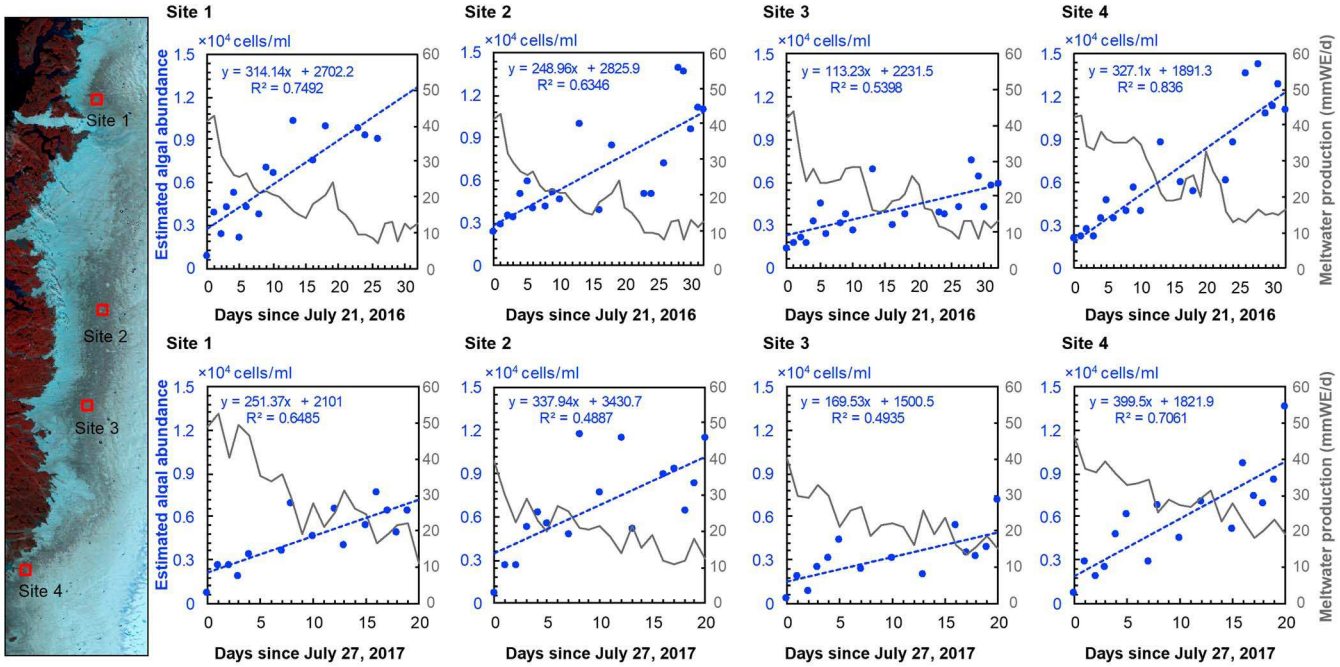

Figure 3. Temporal development of algal abundance (left *y* axis, blue dots, and fitted linear lines and equations), with meltwater production modeled by Modèle Atmosphérique Régionale (right *y* axis and gray lines).

3.3. Ice Algal Development

Figure 3 shows the temporal development of algal abundance over four dark ice sites. We use the dates of maximum dark ice presence, 21 July 2016 and 27 July 2017, as the beginning time of algal population growth, considering the impacts of snow burial and hydrological flushing events on algal distribution (Cameron et al., 2017; Stibal et al., 2017). According to the MAR time series (Figures 1f and 1g), the selected periods plotted in Figure 3 were less affected by snowfall or rainfall events. Our results point to a significant linearly increasing trend of algal abundance with time. This temporal variation pattern is consistent with Stibal et al. (2017) showing that algal population increases as a function of time since last precipitation event based on field measurements.

We further estimated the doubling time for algal population using the fitted linear equations. The average doubling time over the four sites was 11.3 ± 5.2 days during the 2016 summer and 7.9 ± 2.1 days during the 2017 summer. As a comparison, an average doubling time of 5.5 ± 1.7 days was reported by Stibal et al. (2017). Williamson et al. (2018) estimated a doubling time of 7.18 ± 1.04 days for high biomass ice. The longer doubling time in 2016 can be attributed to a larger base number of algal cells on 21 July. In this year, the presence of dark ice at those four sites started before 15 July (Figure S1), suggesting that ice algae had rapidly colonized before 21 July despite the rainfall events. As the algal proliferation progresses, the colonization of algal assemblages would slow down due to limited availability of nutrients and water, in contrast with a rapid growth rate of algal population at the initial stage.

We examined the correlations of algal abundance with surface mass balance and meteorological variables using the estimated daily algal abundance and MAR outputs over those four sites. Regarding the local development of ice algae over time, the algal abundance is negatively correlated with meltwater production and surface runoff (Figure S6), while correlations with other variables are not significant. The negative relationship appears to contradict the fact that liquid water is a prerequisite for algal proliferation. Nevertheless, this counterintuitive result can be explained from following perspectives. First, excessive meltwater and associated high surface runoff could wash out the algal cells or dilute the chlorophyll-*a* concentration, as also reported for other glaciers (Takeuchi, 2001; Uetake et al., 2010). This hypothesis is further supported by the observed altitudinal pattern of algal abundance, that is, the higher elevation areas with less meltwater experienced a higher algal abundance as well. The anticorrelation with meltwater

production and surface runoff is consistent with the fact that algae blooms tend to occur in quiescent or stagnant water (Snoeijs & Prentice, 1989). Second, underestimation of meltwater production by MAR could possibly play a role in the observed negative correlation. Surface albedo is a key parameter for estimating meltwater production based on the surface energy balance. In MAR, the albedo values for bare ice are controlled by the amount of accumulated surface meltwater, whereas the albedo reduction effects caused by dust and biological impurities are not yet considered. There is a positive bias in bare ice albedo simulated by MAR as compared to the MODIS albedo products (Alexander et al., 2014). However, this factor is probably less dominant, given the overall negative trend in insolation and thus the decreasing meltwater production during the analysis period.

4. Discussions and Conclusions

In this study, we demonstrate the capacity of Sentinel-3 OLCI to map the distribution of dark ice and quantify the abundance of ice algae. Although previous studies have attempted to use remote sensing data such as Satellite Pour l'Observation de la Terre multispectral images (Takeuchi et al., 2006) and Airborne Visible/Infrared Imaging Spectrometer hyperspectral images (Painter et al., 2001) to quantify algal biomass on snow and ice surfaces at large spatial scales, the spectral wavelengths and bandwidths of previous satellite sensors are insufficient to detect the narrow spectral signals associated with ice algae, and the availability of airborne hyperspectral data is very limited over Greenland. OLCI is specifically designed for retrieving the content of chlorophylls, phycocyanin, colored dissolved organic matter, etc. in complex water systems. The bands of 665, 673, 681, and 709 nm with narrow bandwidths are sensitive to the chlorophyll content of algal assemblages. The 673-nm channel was particularly added to improve chlorophyll fluorescence measurement as compared to the Envisat Medium Resolution Imaging Spectrometer. Besides, the twin of Senitinel-3A, Sentinel-3B, was successfully placed in orbit in April 2018, thus providing more frequent observations for Greenland.

We use a two-band-algorithm based on the reflectance ratios of 709 and 673-nm bands to characterize the spatial pattern of algal abundance. Through comparison with field measurements, this ratio was demonstrated to be effective as a proxy for algal abundance. A significant exponential relationship was found between the reflectance ratio derived from OLCI data and the algal abundance measured in situ (Stibal et al., 2015, 2017; Williamson et al., 2018). Owing to the recurring nature of ice algae in the same geographic areas (Takeuchi et al., 2006), we estimated the algal abundance over dark ice using the established relationship. The bands of 673 and 709 nm were selected because the spectral signatures of chlorophyll-*a* at these two bands were both present on the OLCI and in situ spectra (Stibal et al., 2017). The spectral characteristics of chlorophylls and carotenoid at the wavelength range of 400–640 nm were not utilized for the following reasons. First, the spatial resolution of OLCI images is 300 m, and each pixel might be mixed with snow, ice, dirt, algae, water, and so on. The spectral signatures of chlorophylls and carotenoid at this spectrum range could be contaminated by the high reflectances of snow and ice. Second, dirt resembles the spectral signatures of carotenoid (Painter et al., 2001; Takeuchi et al., 2006). In contrast, the reflectance features around 670 and 710 nm are uniquely chlorophyll-related and less influenced by snow and ice than shorter wavelengths (Painter et al., 2001).

The processes driving GrIS darkening have been extensively analyzed and discussed (Shimada et al., 2016; Stibal et al., 2017; Tedesco, Box, et al., 2016; Tedesco, Doherty, et al., 2016; Tedstone et al., 2017; Wientjes & Oerlemans, 2010; Yallop et al., 2012). There is growing evidence indicating the ice algal blooms as an important driver for the surface darkening in southwest Greenland (Ryan et al., 2018; Stibal et al., 2017; Williamson et al., 2018). The other processes, including black carbon deposition, outcropping dust in ablating ice, and cryoconite holes, are inadequate to explain the interannual variability of dark ice (Tedesco, Box, et al., 2016; Tedesco, Doherty, et al., 2016; Tedstone et al., 2017). Nonetheless, ice algal growth is controlled by nutrients, liquid water, and sunlight. Phosphorous has been detected from the supraglacial water containing outcropping dust melted from ancient ice (Stibal et al., 2009; Wientjes et al., 2011), and field sampling analysis revealed that the microbial abundance was significantly correlated with the dust content (Stibal et al., 2017). The spatial extent of dark ice and associated algal blooms are very likely to be constrained by the spatial distribution of dust. Our analyses indicate that the dark ice area has strong correlations with surface runoff, suggesting that the runoff of meltwater or rainwater could transport or distribute nutrients and liquid

water required for algal colonization. The linear growth pattern of algal population with time is also consistent with the nature of ice algal bloom development.

We conclude that the Sentinel-3 satellites can effectively capture the dynamics of dark ice and the development of ice algal blooms at a regional scale with a high temporal resolution. Future research should be directed toward (1) combination of Sentinel-3 data with coincident field surveys for more accurate quantification of algal biomass at large spatial scales, (2) quantification of the impacts on surface albedo caused by the development of ice algal blooms in ablation area, and (3) incorporation of bio-albedo effect (Cook et al., 2017) into regional climate models for better projection of future surface mass balance.

Acknowledgments
This work was supported by NSF award ANS 1713072, NASA Exobiology award 80NSSC18K0814, and NASA MAP 80NSSC17K0351. The Sentinel-3 OLCI level-1B data are freely available on the Copernicus Open Access Hub (https://scihub.copernicus.eu/), courtesy of the European Space Agency. The MODIS MOD09GA and MOD10A1 data can be accessed from the NASA Land Processes Distributed Active Archive Center (https://search.earthdata.nasa.gov/). We also thank Xavier Fettweis for his contribution of MAR regional climate model outputs (ftp://ftp.climato.be/fettweis/). The data derived in this study are available as a supporting information data set.

References

Alexander, P. M., Tedesco, M., Fettweis, X., van de Wal, R. S. W., Smeets, C. J. P. P., & van den Broeke, M. R. (2014). Assessing spatio-temporal variability and trends in modelled and measured Greenland ice sheet albedo (2000–2013). *The Cryosphere*, *8*(6), 2293–2312. https://doi.org/10.5194/tc-8-2293-2014

Anderson, G. P., Felde, G. W., Hoke, M. L., Ratkowski, A. J., Cooley, T. W., Chetwynd, J. H., et al. (2002). MODTRAN4-based atmospheric correction algorithm: FLAASH (fast line-of-sight atmospheric analysis of spectral hypercubes). In *Algorithms and technologies for multispectral, hyperspectral, and ultraspectral imagery VIII* (Vol. 4725, pp. 65–72). Orlando, FL: International Society for Optics and Photonics.

Beck, R., Zhan, S., Liu, H., Tong, S., Yang, B., Xu, M., et al. (2016). Comparison of satellite reflectance algorithms for estimating chlorophyll-*a* in a temperate reservoir using coincident hyperspectral aircraft imagery and dense coincident surface observations. *Remote Sensing of Environment*, *178*(Supplement C), 15–30. https://doi.org/10.1016/j.rse.2016.03.002

Blackburn, G. A. (2007). Hyperspectral remote sensing of plant pigments. *Journal of Experimental Botany*, *58*(4), 855–867. https://doi.org/10.1093/jxb/erl123

Blondeau-Patissier, D., Gower, J. F. R., Dekker, A. G., Phinn, S. R., & Brando, V. E. (2014). A review of ocean color remote sensing methods and statistical techniques for the detection, mapping and analysis of phytoplankton blooms in coastal and open oceans. *Progress in Oceanography*, *123*, 123–144. https://doi.org/10.1016/j.pocean.2013.12.008

Box, J. E., Fettweis, X., Stroeve, J. C., Tedesco, M., Hall, D. K., & Steffen, K. (2012). Greenland ice sheet albedo feedback: Thermodynamics and atmospheric drivers. *The Cryosphere*, *6*(4), 821–839. https://doi.org/10.5194/tc-6-821-2012

Cameron, K. A., Stibal, M., Hawkings, J. R., Mikkelsen, A. B., Telling, J., Kohler, T. J., et al. (2017). Meltwater export of prokaryotic cells from the Greenland ice sheet. *Environmental Microbiology*, *19*(2), 524–534. https://doi.org/10.1111/1462-2920.13483

Chandler, D. M., Alcock, J. D., Wadham, J. L., Mackie, S. L., & Telling, J. (2015). Seasonal changes of ice surface characteristics and productivity in the ablation zone of the Greenland ice sheet. *The Cryosphere*, *9*(2), 487–504. https://doi.org/10.5194/tc-9-487-2015

Cook, J. M., Hodson, A. J., Taggart, A. J., Mernild, S. H., & Tranter, M. (2017). A predictive model for the spectral "bioalbedo" of snow. *Journal of Geophysical Research: Earth Surface*, *122*, 434–454. https://doi.org/10.1002/2016JF003932

De Ridder, K., & Gallée, H. (1998). Land surface–induced regional climate change in southern Israel. *Journal of Applied Meteorology*, *37*(11), 1470–1485. https://doi.org/10.1175/1520-0450(1998)037<1470:LSIRCC>2.0.CO;2

Dee, D. P., Uppala, S. M., Simmons, A. J., Berrisford, P., Poli, P., Kobayashi, S., et al. (2011). The ERA-Interim reanalysis: Configuration and performance of the data assimilation system. *Quarterly Journal of the Royal Meteorological Society*, *137*(656), 553–597. https://doi.org/10.1002/qj.828

Fettweis, X., Box, J., Agosta, C., Amory, C., Kittel, C., Lang, C., et al. (2017). Reconstructions of the 1900–2015 Greenland ice sheet surface mass balance using the regional climate MAR model. *The Cryosphere*, *11*(2), 1015–1033. https://doi.org/10.5194/tc-11-1015-2017

Fettweis, X., Franco, B., Tedesco, M., van Angelen, J. H., Lenaerts, J. T. M., van den Broeke, M. R., & Gallée, H. (2013). Estimating the Greenland ice sheet surface mass balance contribution to future sea level rise using the regional atmospheric climate model MAR. *The Cryosphere*, *7*(2), 469–489. https://doi.org/10.5194/tc-7-469-2013

Gallée, H., & Schayes, G. (1994). Development of a three-dimensional Meso-γ primitive equation model: Katabatic winds simulation in the area of Terra Nova Bay, Antarctica. *Monthly Weather Review*, *122*(4), 671–685. https://doi.org/10.1175/1520-0493(1994)122<0671:DOATDM>2.0.CO;2

Gitelson, A. (1992). The peak near 700 nm on radiance spectra of algae and water: Relationships of its magnitude and position with chlorophyll concentration. *International Journal of Remote Sensing*, *13*(17), 3367–3373. https://doi.org/10.1080/01431169208904125

Gitelson, A. A., Gurlin, D., & Moses, W. J. (2009). A bio-optical algorithm for the remote estimation of the chlorophyll-*a* concentration in case 2 waters. *Environmental Research Letters*, *4*(4), 045003. https://doi.org/10.1088/1748-9326/4/4/045003

Goelles, T., & Bøggild, C. E. (2017). Albedo reduction of ice caused by dust and black carbon accumulation: A model applied to the K-transect, West Greenland. *Journal of Glaciology*, *63*(242), 1063–1076. https://doi.org/10.1017/jog.2017.74

Gower, J., King, S., Borstad, G., & Brown, L. (2005). Detection of intense plankton blooms using the 709 nm band of the MERIS imaging spectrometer. *International Journal of Remote Sensing*, *26*(9), 2005–2012. https://doi.org/10.1080/01431160500075857

Hanna, E., Navarro, F. J., Pattyn, F., Domingues, C. M., Fettweis, X., Ivins, E. R., et al. (2013). Ice-sheet mass balance and climate change. *Nature*, *498*(7452), 51–59. https://doi.org/10.1038/nature12238

Howat, I. M., Negrete, A., & Smith, B. E. (2014). The Greenland Ice Mapping Project (GIMP) land classification and surface elevation data sets. *The Cryosphere*, *8*(4), 1509–1518. https://doi.org/10.5194/tc-8-1509-2014

Malenovský, Z., Rott, H., Cihlar, J., Schaepman, M. E., García-Santos, G., Fernandes, R., & Berger, M. (2012). Sentinels for science: Potential of Sentinel-1, -2, and -3 missions for scientific observations of ocean, cryosphere, and land. *Remote Sensing of Environment*, *120*, 91–101. https://doi.org/10.1016/j.rse.2011.09.026

Matthews, M. W. (2011). A current review of empirical procedures of remote sensing in inland and near-coastal transitional waters. *International Journal of Remote Sensing*, *32*(21), 6855–6899. https://doi.org/10.1080/01431161.2010.512947

Painter, T. H., Duval, B., Thomas, W. H., Mendez, M., Heintzelman, S., & Dozier, J. (2001). Detection and quantification of snow algae with an airborne imaging spectrometer. *Applied and Environmental Microbiology*, *67*(11), 5267–5272. https://doi.org/10.1128/AEM.67.11.5267-5272.2001

Remias, D., Schwaiger, S., Aigner, S., Leya, T., Stuppner, H., & Lütz, C. (2012). Characterization of an UV- and VIS-absorbing, purpurogallin-derived secondary pigment new to algae and highly abundant in *Mesotaenium berggrenii* (Zygnematophyceae, Chlorophyta), an extremophyte living on glaciers. *FEMS Microbiology Ecology*, *79*(3), 638–648. https://doi.org/10.1111/j.1574-6941.2011.01245.x

Ruddick, K. G., Gons, H. J., Rijkeboer, M., & Tilstone, G. (2001). Optical remote sensing of chlorophyll *a* in case 2 waters by use of an adaptive two-band algorithm with optimal error properties. *Applied Optics*, *40*(21), 3575–3585. https://doi.org/10.1364/AO.40.003575

Ryan, J. C., Hubbard, A., Stibal, M., Irvine-Fynn, T. D., Cook, J., Smith, L. C., et al. (2018). Dark zone of the Greenland ice sheet controlled by distributed biologically-active impurities. *Nature Communications*, *9*(1), 1065. https://doi.org/10.1038/s41467-018-03353-2

Shepherd, A., Ivins, E. R., A, G., Barletta, V. R., Bentley, M. J., Bettadpur, S., Briggs, K. H., et al. (2012). A reconciled estimate of ice-sheet mass balance. *Science*, *338*(6111), 1183–1189. https://doi.org/10.1126/science.1228102

Shimada, R., Takeuchi, N., & Aoki, T. (2016). Inter-annual and geographical variations in the extent of bare ice and dark ice on the Greenland ice sheet derived from MODIS satellite images. *Frontiers of Earth Science*, *4*, 2293.

Smith, L. C., Chu, V. W., Yang, K., Gleason, C. J., Pitcher, L. H., Rennermalm, A. K., et al. (2015). Efficient meltwater drainage through supraglacial streams and rivers on the Southwest Greenland ice sheet. *Proceedings of the National Academy of Sciences of the United States of America*, *112*(4), 1001–1006. https://doi.org/10.1073/pnas.1413024112

Snoeijs, P. J. M., & Prentice, I. C. (1989). Effects of cooling water discharge on the structure and dynamics of epilithic algal communities in the northern Baltic. *Hydrobiologia*, *184*(1-2), 99–123. https://doi.org/10.1007/BF00014306

Stibal, M., Anesio, A. M., Blues, C. J. D., & Tranter, M. (2009). Phosphatase activity and organic phosphorus turnover on a high Arctic glacier. *Biogeosciences*, *6*(5), 913–922. https://doi.org/10.5194/bg-6-913-2009

Stibal, M., Box, J. E., Cameron, K. A., Langen, P. L., Yallop, M. L., Mottram, R. H., et al. (2017). Algae drive enhanced darkening of bare ice on the Greenland ice sheet. *Geophysical Research Letters*, *44*, 11,463–11,471. https://doi.org/10.1002/2017GL075958

Stibal, M., Gözdereliler, E., Cameron, K. A., Box, J. E., Stevens, I. T., Gokul, J. K., et al. (2015). Microbial abundance in surface ice on the Greenland ice sheet. *Frontiers in Microbiology*, *6*, 225.

Stroeve, J. (2001). Assessment of Greenland albedo variability from the advanced very high resolution radiometer Polar Pathfinder data set. *Journal of Geophysical Research*, *106*(D24), 33,989–34,006. https://doi.org/10.1029/2001JD900072

Takeuchi, N. (2001). The altitudinal distribution of snow algae on an Alaska glacier (Gulkana Glacier in the Alaska Range). *Hydrological Processes*, *15*(18), 3447–3459. https://doi.org/10.1002/hyp.1040

Takeuchi, N., Dial, R., Kohshima, S., Segawa, T., & Uetake, J. (2006). Spatial distribution and abundance of red snow algae on the Harding Icefield, Alaska derived from a satellite image. *Geophysical Research Letters*, *33*, L21502. https://doi.org/10.1029/2006GL027819

Tedesco M., Box J. E., Cappelen J., Fausto R. S., Fettweis X., Hansen K., et al. (2017). Greenland ice sheet [in Arctic report card 2017]. Retrieved from ftp://ftp.oar.noaa.gov/arctic/documents/ArcticReportCard_full_report2017.pdf

Tedesco M., Box J. E., Cappelen J., Fausto R. S., Fettweis X., Mote T., et al. (2016). Greenland ice sheet [in Arctic report card 2016]. Retrieved from ftp://ftp.oar.noaa.gov/arctic/documents/ArcticReportCard_full_report2016.pdf

Tedesco, M., Doherty, S., Fettweis, X., Alexander, P., Jeyaratnam, J., & Stroeve, J. (2016). The darkening of the Greenland ice sheet: Trends, drivers, and projections (1981–2100). *The Cryosphere*, *10*(2), 477–496. https://doi.org/10.5194/tc-10-477-2016

Tedesco, M., Fettweis, X., van den Broeke, M. R., van de Wal, R. S. W., Smeets, C. J. P., van de Berg, W. J., et al. (2011). The role of albedo and accumulation in the 2010 melting record in Greenland. *Environmental Research Letters*, *6*(1), 014005. https://doi.org/10.1088/1748-9326/6/1/014005

Tedstone, A. J., Bamber, J. L., Cook, J. M., Williamson, C. J., Fettweis, X., Hodson, A. J., & Tranter, M. (2017). Dark ice dynamics of the south-west Greenland ice sheet. *The Cryosphere*, *11*(6), 2491–2506. https://doi.org/10.5194/tc-11-2491-2017

Uetake, J., Naganuma, T., Hebsgaard, M. B., Kanda, H., & Kohshima, S. (2010). Communities of algae and cyanobacteria on glaciers in west Greenland. *Polar Science*, *4*(1), 71–80. https://doi.org/10.1016/j.polar.2010.03.002

Warren, S. G. (1982). Optical properties of snow. *Reviews of Geophysics*, *20*(1), 67. https://doi.org/10.1029/RG020i001p00067

Wientjes, I. G. M., de Wal, R. S. W. V., Reichart, G. J., Sluijs, A., & Oerlemans, J. (2011). Dust from the dark region in the western ablation zone of the Greenland ice sheet. *The Cryosphere*, *5*(3), 589–601. https://doi.org/10.5194/tc-5-589-2011

Wientjes, I. G. M., & Oerlemans, J. (2010). An explanation for the dark region in the western melt zone of the Greenland ice sheet. *The Cryosphere*, *4*(3), 261–268. https://doi.org/10.5194/tc-4-261-2010

Williamson, C. J., Anesio, A. M., Cook, J., Tedstone, A., Poniecka, E., Holland, A., et al. (2018). Ice algal bloom development on the surface of the Greenland ice sheet. *FEMS Microbiology Ecology*, *94*(3). https://doi.org/10.1093/femsec/fiy025

Yallop, M. L., Anesio, A. M., Perkins, R. G., Cook, J., Telling, J., Fagan, D., et al. (2012). Photophysiology and albedo-changing potential of the ice algal community on the surface of the Greenland ice sheet. *The ISME Journal*, *6*(12), 2302–2313. https://doi.org/10.1038/ismej.2012.107

Yang, K., & Smith, L. C. (2013). Supraglacial streams on the Greenland ice sheet delineated from combined spectral–shape information in high-resolution satellite imagery. *IEEE Geoscience and Remote Sensing Letters*, *10*(4), 801–805. https://doi.org/10.1109/LGRS.2012.2224316